Full Length Article

# A new thermomechanical coupled FDEM model for geomaterials considering continuum-discontinuum transitions

Zihan Liu, Louis Ngai Yuen Wong*

*Department of Earth Sciences, The University of Hong Kong, Hong Kong China*

## A B S T R A C T

A new thermomechanical (TM) coupled finite-discrete element method (FDEM) model, incorporating heat conduction, thermal cracking, and contact heat transfer, has been proposed for both continuous and discontinuous geomaterials. This model incorporates a heat conduction model that can accurately calculate the thermal field in continuous—discontinuous transition processes within a finite element framework. A modified contact heat transfer model is also included, which accounts for the entire contact area of discrete bodies. To align with the finite strain theory utilized in the FDEM mechanics module, the TM coupling module in the model is based on the multiplicative decomposition of the deformation gradient. The proposed model has been applied to various scenarios, including heat conduction in both continuous and discontinuous media during transient states, thermal-induced strain and stress, and thermal cracking conditions. The thermal field calculation model and the TM coupling model have been validated by comparing the numerical results with experiment findings and analytical solutions. These numerical cases demonstrate the reliability of the proposed model convincingly, making it suitable for use across a wide range of continuous and discontinuous media.

## 1. Introduction

Thermomechanical (TM) coupling has become a significant concern in underground engineering due to its intricate influencing mechanisms. In hot dry rock (HDR) formations, fractures induced by high temperatures play a vital role in maximizing thermal energy extraction efficiency. Likewise, in the field of underground energy storage, comprehending the thermal response of surrounding rock is essential for the design of underground caverns utilized in gas storage systems, compressed air energy storage, and storage of hydrogen or carbon dioxide. In deep geological disposal of radioactive waste, the decay of nuclear materials releases significant heat, causing dynamic temperature fluctuations that affect stress and deformation distribution in the surrounding rocks. The occurrence of fractures is highly undesirable as it creates potential pathways for the transport of radionuclides into the biosphere. Hence, accurate calculation of thermal loads and prediction of thermally induced cracks are of utmost significance for the design,

construction, and safe maintenance of underground space exploitation. Three primary numerical approaches are used to calculate the coupling of TM processes, deformation and fracture in rocks: continuum-based methods, discontinuity-based methods and hybrid approaches. These methods facilitate a comprehensive analysis of the TM response of rocks and assist in informed engineering decision-making. The choice of analysis depends on material characteristics and research objectives.

Continuum-based approaches have played a crucial role in the early stages of thermal fracturing research. The finite element method (FEM) discretizes a domain into small elements, establishes a mathematical model based on node variable vector, stiffness matrices, and external load vector, and solves algebraic equations to calculate the temperature field distribution. Tang et al. (2016) proposed a thermo-damage method under the FEM framework to tackle thermal-induced cracking in brittle solids. However, FEM relies on the assumption of continuum mechanics and faces challenges in accurately representing the behavior of multiple cracks, thereby limiting its effectiveness in simulating thermal fracturing and fragmentation. To overcome these limitations, researchers introduced a continuum approach based on phase field theory, which can account for the brittle fracture development in thermo-elastic-plastic materials (Miehe et al., 2015a, b). While this

* Corresponding author.
*E-mail address:* LNYWONG@hku.hk (L.N.Y. Wong).

approach shows promise, it comes with the limitation of requiring ultra-fine meshing to accurately represent the fracture topology, which subsequently leads to substantial computational expenses (Li et al., 2022). Furthermore, the phase field method, being a continuous approach, does not provide an explicit representation of cracks, which could potentially lead to inaccurate calculations of crack velocity in dynamic fracture situations. In contrast, the peri-dynamic method offers a significant advantage, as its governing equation remains effective even across discontinuities. Wang et al. (2018) proposed a TM coupling model for rocks, aiming to study the thermal cracking problems based on peridynamics theory. However, it is worth noting that conventional peridynamic models exhibit higher computational costs compared to methods based on classical theories, primarily due to their inherent nonlocal nature (Bazazzadeh et al., 2020). Numerical methods specialized in the study of fracture problems, for instance, the boundary element method and its extension, i.e. dual boundary element method and displacement discontinuity method (Abdollahipour et al., 2016a, b; Haeri et al., 2013), are further developed to incorporate coupling effects (Giannopoulos and Anifantis, 2005; Rinne et al., 2013). Abdollahipour and Fatehi Marji (2020) proposed a thermo-hydromechanical model based on the displacement discontinuity method to couple the fracturing, temperature, and fluid pressure effects. Besides, the extended finite element method (Fu et al., 2022) is also a promising method for deep underground engineering that has been modified to consider the influence of temperature (Liu et al., 2014; Zeng et al., 2020). Despite their advancements, these approaches do not account for the impact of thermal contacts of discontinuous materials, such as the interaction between fracture walls or heat resistance arising from contact between discrete parts.

To address the constraints of continuum-based approaches, discontinuous-based approaches have gained significant attention for simulating thermal cracking in geomaterials. The discrete element method (DEM) is a prominent example of these approaches. By introducing a thermal conduction module into the bonded-particle model, thermal fracturing simulation in geomaterials was realized by Xia (2015) for circular particles and by André et al. (2017) for spherical particles. However, most of the current particle-based DEM models adopt excessively simplistic isothermal assumptions. In addition, these models have used circular/spherical particles, with their outcomes influenced by the particle size and the structural distribution characteristics of the particles in the numerical model, and the contact area calculation remains a complex problem.

Block-based DEM, such as the universal distinct element code (UDEC), presents additional challenges for simulating heat transfer between elements since subdividing contact zones may introduce computational inaccuracies and necessitate very small time-steps in temperature field calculations. Discontinuous deformation analysis (DDA) employs discrete blocks and joints to model temperature field interactions (Shahami et al., 2019), allowing for the simulation and calculation of temperature distributions in complex geomechanical systems. Jiao et al. (2015) proposed a TM coupling model to investigate the thermal stress-induced fracturing in rocks within the DDA framework. To reduce the extensive contact analysis in DDA, Choo et al. (2016) proposed a combined DDA-FEM that used FEM mesh for major parts of domain and only a few DDA blocks are required. As a result, the computational cost is reduced by a large amount since only the block boundaries require contact analysis (Choo et al., 2016). Nevertheless, DDA methods treat heat conduction calculations separately from the mechanical calculations. Even when cracks have formed, the calculation mesh used for heat conduction still retains shared nodes along the cracks (Yan et al., 2021a). As a result, the temperature across the cracks

remains consistent, and the impact of cracking on the temperature field is not accounted for. Furthermore, it is essential to calibrate the DEM microscopic parameters to match the macroscopic mechanical and thermal properties of the material before conducting formal numerical simulations, which remains a challenge for researchers.

In contrast to the aforementioned approaches, the combined finite-discrete element method (FDEM) is a novel method that integrates continuum mechanics concepts with DEM algorithms (Munjiza et al., 1995; Mahabadi et al., 2012; Zhao et al., 2014). FDEM is an ideal numerical approach to capture progressive damage and failure processes in brittle materials, which makes it a suitable numerical solution to deep underground engineering applications, such as HDR geothermal systems, deep oil reservoirs, and geological disposal of radioactive waste (Sun et al., 2022; Cai et al., 2023; Wang et al., 2021). Taking HDR geothermal systems as an example, it involves three major steps, i.e. reservoir reconstruction, cold water injection, and hot water (steam) extraction. The injection pressure and the large temperature differences between the injection water and the reservoir will possibly generate fractures in the host rocks (Cui and Wong, 2022). Benefiting from the nature of FDEM, it can accurately simulate the fracturing behavior in reservoir reconstruction and production of HDR systems. Besides, by using a TM coupled FDEM model, heat transfer calculations in both continuous and discontinuous media can be performed, while also addressing the continuum-discontinuum transition process. Therefore, the evolution of fracture state in reservoirs can be simulated during production.

Based on FDEM, Yan and Zheng (2017), Yan et al. (2019a, b), and Yan and Jiao (2020) proposed several TM coupling models for thermal fracturing simulation in geomaterials. Nevertheless, heat conduction is only considered within a single solid in these approaches, while the heat transfer during contact is ignored, which limits their utilization in discontinuous geomaterials. Yan et al. (2021b) subsequently developed a thermal contact algorithm based on earlier heat conduction FDEM models. However, the above-mentioned TM coupled FDEM models predominantly rely on the small strain assumption, which is inadequate for handling large deformation issues. To address these limitations, researchers (Joulin et al., 2020a; Wang et al., 2021) proposed thermal stress expression under the finite deformation configuration, which can function in large deformation FDEM simulations with thermal fracturing. It is worth noting that the studies mentioned above predominantly applied a discrete equation system to independently calculate the temperature of nodes in computational domains. This approach does not align with the continuum characteristic of heat conduction in intact rocks, potentially leading to inaccuracies in the temperature field. Joulin et al. (2020b) utilized a thermal field calculation model comprising two independent parts: a FEM-based heat conduction module for continuum and a DEM-based heat contact module for discontinuum. However, this method is unable to handle the continuous-discontinuous transition processes in thermal field calculation under quasi-static and dynamic conditions. Therefore, a heat conduction/contact approach that considers the continuous-discontinuous transition process should be developed to achieve the TM coupling simulation of the rock deformation − fracture − failure process. Additionally, current heat transfer calculations for thermal contact are mainly based on a single edge of the contact area, rather than the entire overlapping region (Wang et al., 2021; Yan et al., 2021b). This approach may introduce severe inaccuracies when applied to multi-body contact simulations in geomaterial particles or discontinuum.

To address the aforementioned challenges, this study proposes a new thermal field calculation scheme and an overlapping region-based contact heat transfer algorithm. These advancements will

contribute to achieving the TM coupling simulation of rock deformation, fracture, and the failure process. The rest of this paper is structured as follows. Section 2 provides a brief overview of the FDEM theory. Section 3 introduces the new heat transfer model for FDEM. The TM coupling model is presented in Section 4. Finally, a few numerical verification examples are shown in Section 5.

## 2. Overview of the FDEM

The computational domain in the FDEM approach is discretized into solid elements and joint elements without thickness. Within this framework, solid elements exclusively undergo elastic deformation, and their computational process is conducted under the finite element framework. Conversely, damage and fracture occur exclusively in joint elements, which are governed by cohesive zone models. The no binary search (NBS) algorithm and a contact force calculation method based on the potential-based penalty function approach are employed to address discrete elements (Munjiza and Andrews, 1998). Only a concise overview of the FDEM is provided here, with comprehensive and in-depth explanations of its basic principles available in the literature (Fukuda et al., 2020; Sun et al., 2020; Wu et al., 2022, 2023).

### 2.1. Governing equation and numerical integration

The governing equation of FDEM is based on Newton's second law, which can be expressed as

$$M\ddot{u} + C\dot{u} + f^{int}(u) = f^{ext} \qquad (1)$$

where $M$ is the mass matrix; $C$ is the damping matrix; and $f^{int}(u)$ and $f^{ext}$ are the internal and external forces, respectively.

The nodal velocity and displacement of solid elements are updated using the explicit central difference approach:

$$\left.\begin{aligned} v_i^{(t+\Delta t)} &= v_i^{(t)} + \frac{\sum F_i^{(t)}}{m}\Delta t \\ x_i^{(t+\Delta t)} &= x_i^{(t)} + v_i^{(t)}\Delta t \end{aligned}\right\} \qquad (2)$$

where $\sum F_i^{(t)}$ is the total nodal force, $m$ is the nodal mass, and $\Delta t$ is the time interval.

### 2.2. Constitutive model of the joint element

In FDEM, the yield and failure status of a joint element is determined by its deformation, i.e. joint opening $o$ and joint slip $s$. Typical failure modes include Mode I (tension, opening), Mode II (shear, sliding), and mixed Mode I-II:

(1) Mode I failure. In the original state, the opening of joint elements is a negative value, indicating that the joint elements are in a compression state. With the gradual increase of opening, the normal cohesive force rises accordingly. The critical value $o_p$ of the opening occurs when the normal cohesive force attains its maximum, which corresponds to the tensile strength of the joint, $f_t$. Subsequently, the joint element undergoes a yield state. When the opening reaches the residual opening $o_r$, the joint element fails and forms a tensile fracture.

(2) Mode II failure. With the increasing sliding displacement, the tangential cohesive force rises accordingly and reaches its maximum, corresponding to the peak shear strength of the joint, when $s$ reaches the critical value $s_p$. When the sliding

displacement is larger than $s_p$, the joint element enters a yield state. Once the sliding displacement reaches $s_r$, shear failure occurs, and the tangential cohesive force decreases to the residual shear strength.

(3) Mixed Mode I-II failure. Except for Mode I and Mode II failure, when the joint displacement is smaller than $o_r$ and $s_r$, mixed Mode I-II failure occurs, and the residual displacement can be very significant. Therefore, an elliptical function is utilized to govern the mixed failure mode subjected to both tensile and shear stresses simultaneously:

$$\left(\frac{o - o_p}{o_r - o_p}\right)^2 + \left(\frac{s - s_p}{s_r - s_p}\right)^2 \geq 1 \qquad (3)$$

### 2.3. Contact detection and contact force

The NBS algorithm (Munjiza and Andrews, 1998) can be explained as follows: First, the two-dimensional (2D) computational domain is meshed into numerous equal-sized square cells. Next, each discrete element is mapped to its corresponding square cell, and contact detection is performed only within that specific square cell and its adjacent cells. This approach eliminates unnecessary contact detection between distant elements, significantly improving computational efficiency.

FDEM incorporates a distributed contact force approach that considers the size and shape of the overlapping boundary between contact pairs. In this context, a contact element and a target element form a contact pair, while the overlapping area is denoted as $S$. A potential function is defined for triangular elements. The potential of any point $P$ in a triangular element is shown below:

$$\varphi(P) = \min\left(\frac{3A_1}{A}, \frac{3A_2}{A}, \frac{3A_3}{A}\right) \qquad (4)$$

where $A_i$ ($i = 1, 2, 3$) denotes the area of the corresponding sub-triangle shown in Fig. 1; and $\varphi$ equals one at the centroid and zero on the boundary.

For an infinitesimal area $dA$ on the contact area, the potential differs between the contact and target elements. Based on the
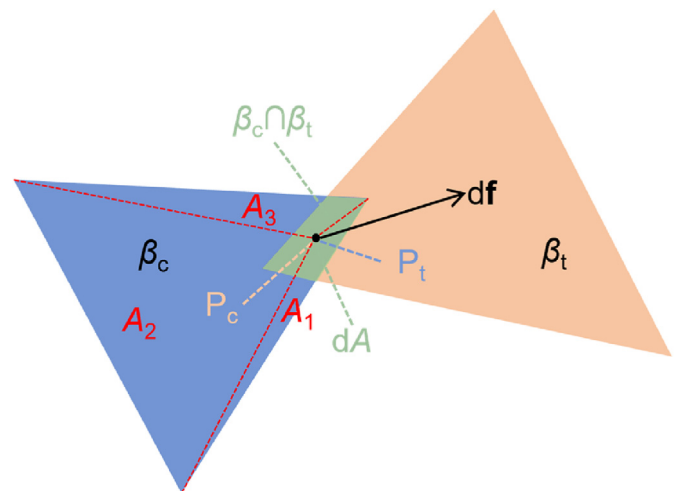


**Fig. 1.** Schematic diagram of the potential and contact force.

potential difference between these two elements, the contact force of d$A$ from the target element to the contact element is as follows:

$$df_n = p_n(\text{grad}\varphi_c(P_c) - \text{grad}\varphi_t(P_t))dA \tag{5}$$

where d$f_n$ is the normal contact force generated by d$A$; grad denotes the gradient; $p_n$ is the normal contact penalty parameter; $P_c$ and $P_t$ are the positions of d$A$ in the contact and target elements, respectively; and $\varphi_c$ and $\varphi_t$ are the potentials at the point in the contact and target elements, respectively. By integrating Eq. (5) over the entire overlapped area, the total contact force of the entire contact area can be calculated.

The relative displacement of the interaction edge between the contact element and target element is the sliding distance $\delta_s$. Its initial value is zero and gradually increases with the deformation of the computational domain. In triangular elements, the tangential contact force depends on tangential penalty parameters $p_r$ and $\delta_s$ in the beginning. When $\delta_s$ reaches a critical value, the tangential contact force is determined according to Coulomb friction as follows:

$$f_t = \frac{\delta_s}{|\delta_s|}\min(p_r h|\delta_s|, \sigma_n f_r) \tag{6}$$

where $h$ is the element edge length, $\sigma_n$ is the normal force on interaction edge, and $f_r$ is the frictional coefficient.

## 3. Heat transfer model for FDEM

### 3.1. Basic theory for heat conduction

Fourier's law of heat conduction and the law of conservation of energy are combined to create the thermal diffusion governing equation:

$$\rho c_p \frac{\partial T}{\partial t} = -\nabla^T q + s = -\begin{bmatrix} \frac{\partial}{\partial x} & \frac{\partial}{\partial y} \end{bmatrix}\begin{bmatrix} q_x \\ q_y \end{bmatrix} + s \tag{7}$$

$$q = \begin{bmatrix} q_x \\ q_y \end{bmatrix} = -\begin{bmatrix} k_{xx} & k_{xy} \\ k_{yx} & k_{yy} \end{bmatrix}\begin{bmatrix} \frac{\partial}{\partial x} \\ \frac{\partial}{\partial y} \end{bmatrix} T = -D\nabla T \tag{8}$$

where $s$ is the heat source, $T$ is the temperature, $t$ is the time, $x$ and $y$ are the coordinates, $k$ is the thermal conductivity, $\rho$ is the density, and $c_p$ is the heat capacity.

Then, we can obtain the following expression:

$$\rho c_p \frac{\partial T}{\partial t} = \nabla^T(D\nabla T) + s \tag{9}$$

This equation is widely used for 2D transient heat conduction. If the thermal conductivity is isotropic and remains unchanged in computational domain, Eq. (9) in 2D is simplified to

$$\frac{\partial T}{\partial t} = \kappa\left(\frac{\partial^2 T}{\partial x^2} + \frac{\partial^2 T}{\partial y^2}\right) + \frac{s}{\rho c_p} \tag{10}$$

where $\kappa = k/(\rho c_p)$ is the thermal diffusivity. The thermal diffusivity matrix of isotropic material is as follows:

$$D = \begin{bmatrix} \kappa & 0 \\ 0 & \kappa \end{bmatrix} \tag{11}$$

### 3.2. Finite element discretization

The computational domain $\Omega$ is discretized into finite elements, and the domain boundary is denoted as $\Gamma$. We choose here the triangular element with the following shape function:

$$N_i(x,y) = \frac{1}{2A_e}(a_i + b_i x + c_i y) \tag{12}$$

where $a_i$, $b_i$, and $c_i$ are the coefficients related to node $i$; and $A_e$ is the area of the element. Using $N$ to represent shape functions of an element, we have

$$N(x,y) = [N_1(x,y) \quad N_2(x,y) \quad N_3(x,y)] \tag{13}$$

Then, the shape function is utilized to map the node variable $T_i$ to the continuous variable $T$:

$$T(x,y) = [N_1(x,y) \quad N_2(x,y) \quad N_3(x,y)]\begin{bmatrix} T_1 \\ T_2 \\ T_3 \end{bmatrix} = NT \tag{14}$$

Substituting $T$ into Eq. (9), we can then obtain the following expression:

$$\rho c_p \frac{\partial}{\partial t}(NT) = \nabla^T(D\nabla N)T + s \tag{15}$$

Multiplying Eq. (15) by the weighting functions and integrating over the computational domain $\Omega^e$ yields

$$\iint_{\Omega^e} \rho c_p N^T \frac{\partial}{\partial t}(NT)dxdy =$$

$$\iint_{\Omega^e} N^T \nabla^T(D\nabla N)Tdxdy + \iint_{\Omega^e} N^T s dxdy \tag{16}$$

Applying integration by parts of the above equation over $\Omega^e$ and applying Green's theorem yields the following expression:

$$\left[\iint_{\Omega^e} \rho c_p N^T N dxdy\right]\frac{\partial T}{\partial t} + \left[\iint_{\Omega^e} \nabla N^T(D\nabla N)dxdy\right]T$$

$$= \iint_{\Omega^e} N^T s dxdy + \oint_{\Gamma^e} N^T \hat{q}^T n ds \tag{17}$$

where $\hat{q}$ is the given heat flux, and $n$ is the outer normal vector. The second item on the right-hand side of Eq. (17) represents the Neumann boundary condition.

The simplified form of Eq. (17) is as follows:

$$M\frac{\partial T}{\partial t} + KT = P \tag{18}$$

where the heat capacity matrix, thermal conductivity matrix, and thermal load vector are as follows:

$$\left.\begin{array}{l} M = \iint_{\Omega^e} \rho c_p N^T N dxdy \\ K = \iint_{\Omega^e} \nabla N^T(D\nabla N)dxdy \\ P = \iint_{\Omega^e} N^T s dxdy + \oint_{\Gamma^e} N^T \hat{q}^T n ds \end{array}\right\} \tag{19}$$

The shape function derivatives are shown below:

$$\nabla \boldsymbol{N}(x,y) = \begin{bmatrix} \dfrac{\partial N_1}{\partial x} & \dfrac{\partial N_2}{\partial x} & \dfrac{\partial N_3}{\partial x} \\ \dfrac{\partial N_1}{\partial y} & \dfrac{\partial N_2}{\partial y} & \dfrac{\partial N_3}{\partial y} \end{bmatrix} \tag{20}$$

To solve the transient heat transfer problem, it is also necessary to discretize the time derivative in Eq. (18) by finite difference method:

$$\boldsymbol{M}\frac{\boldsymbol{T}^{n+1} - \boldsymbol{T}^n}{\Delta t} + \boldsymbol{K}\boldsymbol{T}^{n+1} = \boldsymbol{P} \tag{21}$$

where $\boldsymbol{T}^{n+1}$ is the function value at the next time step $n + 1$, and $\boldsymbol{T}^n$ is the known value at the current time step $n$. Rearranging Eq. (21), we can obtain the following expression:

$$\left(\frac{\boldsymbol{M}}{\Delta t} + \boldsymbol{K}\right)\boldsymbol{T}^{n+1} = \frac{\boldsymbol{M}}{\Delta t}\boldsymbol{T}^n + \boldsymbol{P} \tag{22}$$

In the FDEM model, both the joint heat exchange component and contact heat transfer component are taken into consideration. Joint elements are inserted between the solid elements to account for heat conduction in the material. When heat conduction occurs within the material modeled by the FDEM, the transfer of heat from one element to its neighboring element must pass through the joint element connecting them. As a result, the joint elements play a crucial role in the heat conduction within solid material in the FDEM method. To accurately capture the impact of joint elements, the joint heat exchange component is introduced. This component represents the heat conduction process through the boundaries of solid elements and is incorporated into the global right-hand vector of thermal loads, denoted as $\boldsymbol{P}$.

On the other hand, when two discrete solids with different temperatures contact at a specific region, heat is transferred through their contact area, influencing the heat conduction within the solids. To reflect this mechanism, the contact heat transfer component is added to the global right-hand vector of thermal loads $\boldsymbol{P}$ to reflect the contribution of other solids to the heat conduction.

When a fracture occurs, two solid elements debond and the joint element between them breaks. Simultaneously, the joint heat exchange component also fails, representing the transformation of the heat conduction mode from continuum to discontinuum in the local region. Heat conduction between these two discrete solid elements will occur through contact heat transfer via the contact heat transfer component. Consequently, these two heat conduction components facilitate the entire heat transfer process, transitioning from continuum to discontinuum using the FDEM method.

The global right-hand vector of thermal loads in FDEM method can be written as

$$\boldsymbol{P} = \boldsymbol{P}^{\text{inter}} + \boldsymbol{P}^{\text{ct}} \tag{23}$$

where $\boldsymbol{P}^{\text{inter}}$ is the joint heat exchange component, and $\boldsymbol{P}^{\text{ct}}$ is the contact heat transfer component.

Eq. (23) can be rewritten as the form of the assembly of elements:

$$\left.\begin{aligned} P_i &= \sum_e P_i^{\text{inter}} + \sum_e P_i^{\text{ct}} \\ P_i^{\text{inter}} &= \oint_{\Gamma^e} q_i^{\text{inter}} N_i \mathrm{d}\Gamma \\ P_i^{\text{ct}} &= \oint_{\Gamma^e} q_i^{\text{ct}} N_i \mathrm{d}\Gamma \end{aligned}\right\} \tag{24}$$

### 3.3. Heat transfer between adjacent elements

The joint heat exchange component can be expressed as follows:

$$P_i^{\text{inter}} = \sum_{n=1}^{n_i} p_i^{\text{inter},n} \tag{25}$$

where $n_i$ is the number of joint elements in which node $i$ is involved.

In conventional FEM and similar methods, heat exchange between adjacent solid elements occurs automatically via shared nodes. However, in the FDEM approach, adjacent elements will be separated to enable the modeling of the progressive damage process, resulting in no shared nodes. Instead, these elements transfer heat through joint elements until a fracture occurs.

We assume that there is no loss of heat flow when traversing the discontinuity. The heat flow at the boundary of adjacent elements can be determined:

$$q_i^- = -q_i^+ = k_i\Delta T = k_i(T_i^+ - T_i^-) \tag{26}$$

where $\Delta T$ denotes the temperature difference between two adjacent elements, and $k_i$ represents the interfacial heat conductivity that is utilized to characterize the heat transferring capacity of the discontinuous interface.

The heat flux into the node of the adjacent solid element via the joint element is as follows:

$$p_1^{\text{inter},1234} = \frac{1}{2}\oint_{\Gamma_i} q_i \mathrm{d}\Gamma \tag{27}$$

### 3.4. Heat transfer between contact elements

This section introduces the calculation of heat transfer through contact element pairs. The contact heat transfer component for finite elements is formulated as

$$P_i^{\text{ct}} = \sum_{n=1}^{n_c} p_i^{\text{ct},n} \tag{28}$$

where $n_c$ is the number of times that node $i$ is in contact with other elements.

For an element, the heat flux of unit cross-section area in the $i$ direction is shown below:

$$q_i = -k_{ij}\frac{\partial T}{\partial x_j} \tag{29}$$

Assuming a linear distribution of temperature across the element, the temperature gradient remains constant throughout the element and follows the below expression:

$$\frac{\partial T}{\partial x_j} = \frac{1}{A} \int_A \frac{\partial T}{\partial x_j} dA \tag{30}$$

where $A$ is the contact area.

Applying Gauss's divergence theorem, Eq. (30) can be rewritten as

$$\frac{\partial T}{\partial x_i} = \frac{1}{A} \oint_{\Gamma_i} T n_\mathbf{i} d\Gamma \tag{31}$$

where $\Gamma_i$ is the boundary of the contact area.

The heat flow on the overlapped area of the contact element and target element, $\mathbf{q}_c$ and $\mathbf{q}_t$, are calculated respectively. According to the superposition principle, the local net heat flow is determined as:

$$\mathbf{q} = [q_c \quad q_t] \begin{bmatrix} n_i \\ n_j \end{bmatrix} \tag{32}$$

where $n_i$ and $n_j$ are the outward normal vectors.

The total transferred heat on the contact area is

$$p^{ct} = h_c \int_A \mathbf{q} dA \tag{33}$$

where $h_c$ is the thermal contact conductance coefficient as the non-ideal contact possesses thermal contact resistance.

Contact transferred heat is assigned to the nodes of target ($A$, $B$, $C$) and contact (0, 1, 2) triangular elements by using the shape function. For instance, $N_A$, $N_B$, and $N_C$ are the shape functions of nodes $A$, $B$, and $C$ in the target element, respectively, and meet the following relationship:

$$\left. \begin{array}{l} N_A + N_B + N_C = 1 \\ 0 \le N_A \le 1 \\ 0 \le N_B \le 1 \\ 0 \le N_C \le 1 \end{array} \right\} \tag{34}$$

In this case, we set the barycenter $G$ of the overlapped area as the equivalent action point. Based on the coordinates of $G$, $N_A$, $N_B$, and $N_C$ can be calculated as follows:

$$N_A = \frac{S_{BCG}}{S_{ABC}}, N_B = \frac{S_{ACG}}{S_{ABC}}, N_C = \frac{S_{BAG}}{S_{ABC}} \tag{35}$$

The shape functions of the contact element $N_0$, $N_1$ and $N_2$ are defined similarly to Eq. (35) and calculated with the help of the barycenter $G$.

The allocation of the contact heat to the nodes of the contact element and target element can be calculated as follows:

$$\begin{bmatrix} p_i^{ct,n} \\ p_j^{ct,n} \end{bmatrix} = p^{ct} [N_i \quad N_j] \begin{bmatrix} n_i \\ n_j \end{bmatrix} \quad (i = A, B, C; \ j = 0, 1, 2) \tag{36}$$

## 4. TM coupling model covering thermal fracture

### 4.1. Multiplicative decomposition of deformation gradient

Based on the concept of multiplicative decomposition of the deformation gradient (Vujosevic and Lubarda, 2002), the total deformation gradient $\mathbf{F}$ can be split into a thermal component $\mathbf{F}_T$ and an elastic component $\mathbf{F}_e$:

$$\mathbf{F} = \mathbf{F}_T \mathbf{F}_e \tag{37}$$

where $\mathbf{F}_T$ and $\mathbf{F}_e$ can be expressed as follows (Joulin et al., 2020a; Wang et al., 2021):

$$\left. \begin{array}{l} \mathbf{F}_T = (1 + \alpha \Delta T)\mathbf{I} \\ \mathbf{F}_e = \mathbf{F}_{e,c} + \mathbf{F}_{e,i}^{-1} \end{array} \right\} \tag{38}$$

where $\alpha$ is the thermal expansion coefficient; $\mathbf{I}$ is the identity matrix; and $\mathbf{F}_{e,i}$ and $\mathbf{F}_{e,c}$ are the matrices describing the element bases in the initial and current local frames, respectively:

$$\left. \begin{array}{l} \mathbf{F}_{c,i} = \begin{bmatrix} x_{i1} - x_{i0} & x_{i2} - x_{i0} \\ y_{i1} - y_{i0} & y_{i2} - y_{i0} \end{bmatrix} \\ \\ \mathbf{F}_{e,c} = \begin{bmatrix} x_{c1} - x_{c0} & x_{c2} - x_{c0} \\ y_{c1} - y_{c0} & y_{c2} - y_{c0} \end{bmatrix} \end{array} \right\} \tag{39}$$

Eq. (37) can be rewritten as follows:

$$\mathbf{F} = (1 + \alpha \Delta T)\mathbf{F}_e \tag{40}$$

### 4.2. Thermal stress

The left Cauchy–Green strain tensor $\mathbf{B}$ can be obtained according to the deformation gradient:

$$\mathbf{B} = \mathbf{B}_T \mathbf{B}_e = \mathbf{F} \mathbf{F}^T \tag{41}$$

where $\mathbf{B}_T$ is the thermal component, and $\mathbf{B}_e$ is the elastic component. They can be calculated as

$$\left. \begin{array}{l} \mathbf{B}_T = \mathbf{F}_T \mathbf{F}_T^T \\ \mathbf{B}_e = \mathbf{F}_e \mathbf{F}_e^T \end{array} \right\} \tag{42}$$

We can obtain the Green–St. Venant strain tensor $\mathbf{E}$ based on $\mathbf{B}$ and $\mathbf{I}$:

$$\mathbf{E} = \frac{\mathbf{B} - \mathbf{I}}{2} \tag{43}$$

The Cauchy stress $\mathbf{T}$ can be determined by

$$\mathbf{T} = 2\mu \frac{\det(\mathbf{F}_{e,i})}{\det(\mathbf{F}_{e,c})} \mathbf{E} + \frac{\lambda}{2} \left( \frac{\det(\mathbf{F}_{e,c})}{\det(\mathbf{F}_{e,i})} - \frac{\det(\mathbf{F}_{e,i})}{\det(\mathbf{F}_{e,c})} \right) \mathbf{I} + \mathbf{C}_D \tag{44}$$

where $\mu$ and $\lambda$ are the Lamé coefficients; $\mathbf{C}_D$ is the dissipative component of the stress (Xiang et al., 2009), which can be expressed as

$$\mathbf{C}_D = 2\eta \mathbf{D} \tag{45}$$

where $\eta$ denotes the viscosity; and $\mathbf{D}$ is the rate of deformation matrix and formulated as

$$\mathbf{D} = \frac{\mathbf{L} + \mathbf{L}^T}{2} \tag{46}$$

where $\mathbf{L}$ means the velocity gradient, and $\mathbf{L} = \mathbf{F} \mathbf{F}^{-1}$.

### 4.3. TM coupling process

The flowchart shown in Fig. 2 displays the overall algorithm scheme of the TM coupling model.

For the coupling scheme, it can be divided into two parts:

(1) T→M part
  (i) Temperature changes will induce thermal deformation and thermal stress.
  (ii) Thermal-induced stress may cause thermal fracturing, which may change the mechanical properties of materials.
(2) M→T part
  (i) Given that mechanical changes are assumed to exert a minimal impact on temperature variations, this is based on the understanding that energy alterations in quasi-static mechanical scenarios tend to be negligible (Guo et al., 2023).
  (ii) Fracturing and contacts in the mechanical module will affect the heat transfer process in solid elements and joint elements, and subsequently change the thermal field.
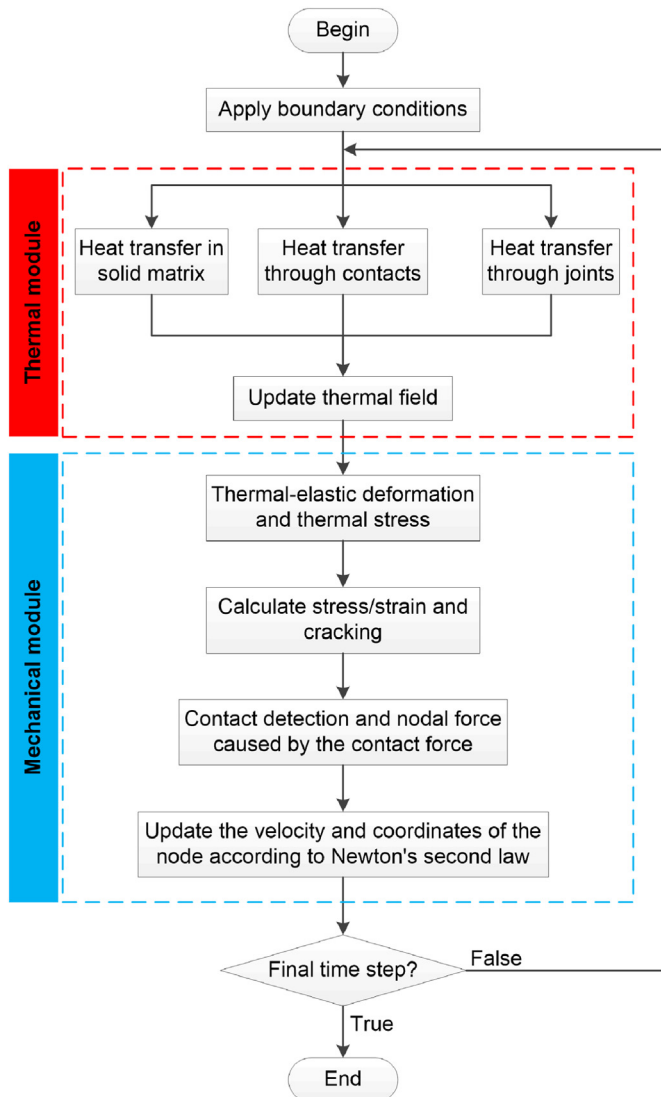


**Fig. 2.** The flowchart of the calculation procedure in the TM-FDEM model.

**Table 1**
Numerical parameters of rectangular plate for transient heat conduction.

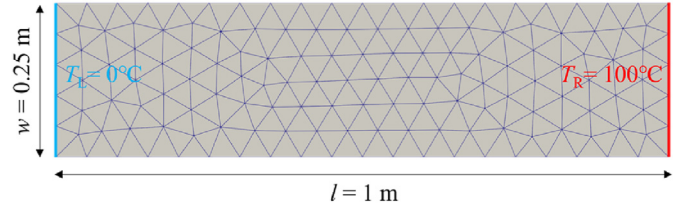| Numerical parameters | Value |
| --- | --- |
| Mesh size (m) | 0.05 |
| Element quantity | 244 |
| Time step (s) | $1 \times 10^{-7}$ |
| Density, $\rho$ (kg/m$^3$) | 2000 |
| Elastic modulus, $E$ (GPa) | 50 |
| Poisson's ratio, $\nu$ | 0.25 |
| Thermal conductivity, $k$ (W/(m °C)) | 10 |
| Heat capacity, $c_p$ (J/(kg °C)) | 1 |



**Fig. 3.** Numerical model setup for heat conduction in transient states.

By using the explicit time integration scheme with fine time-step size, the TM model can precisely capture the interaction between mechanical and thermal fields.

## 5. Verification examples

### 5.1. Heat conduction in transient states

To verify the accuracy of the novel TM model under transient conditions, the temporal variations of temperature in a rectangular plate were examined. A simulation of transient heat conduction was conducted and compared with an analytical solution to assess its reliability. The rectangular plate, with dimensions of 1 m in length and 0.25 m in width, starts with an initial temperature of 0 °C. The left side of the plate maintains a constant 0 °C, while the right boundary is set to a constant 100 °C. The top and bottom boundaries of the model are considered adiabatic. Specific numerical parameters for this case are provided in Table 1, and the numerical model is illustrated in Fig. 3.

The analytical solution for temperature field of this case is shown below:

$$T(x,t) = T_L + (T_R - T_L)\frac{x}{l}$$
$$+ \frac{2}{\pi}\sum_{\pi=1}^{\infty}\left\{\frac{T_R\cos(n\pi) - T_L}{n}\exp\left(\frac{-\kappa n^2\pi^2 t}{l^2}\right)+\right.$$

$$\left.\frac{4T_i}{\pi}\sum_{m=0}^{\infty}\frac{1}{2m+1}\sin\frac{(2m+1)\pi x}{l}\exp\left[\frac{-\kappa(2m+1)^2\pi^2 t}{l^2}\right]\right\} \quad (47)$$

where $x$ is the distance from the left boundary.

The temperature distributions in the rectangular plate during transient states at different time points ($t = 2$ s, 10 s, 20 s, and 50 s) are displayed in Fig. 4a. The heat transfer is observed to occur from the high-temperature end to the low-temperature end, with the heated region expanding gradually over time (from 2 s to 50 s). Fig. 4b illustrates a comparison between numerical and analytical results of the thermal field, revealing excellent agreement and thereby validating the reliability of the present model for modeling the transient TM response.
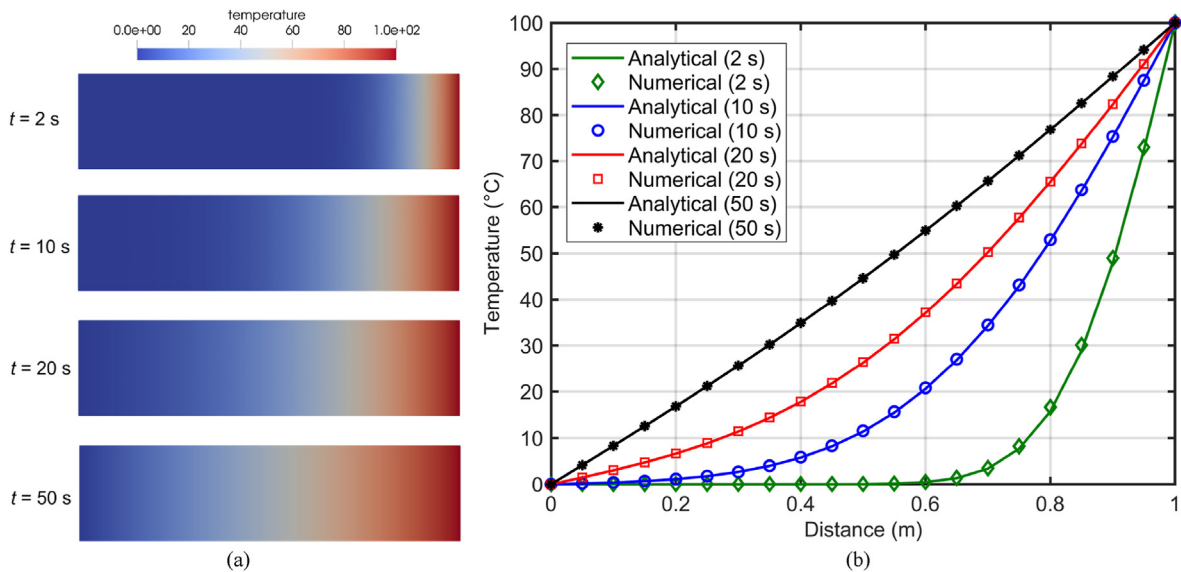
**Fig. 4.** Temperature results in rectangular plate at different times: (a) Temperature fields (in °C); and (b) Comparison between analytical and numerical results.

## 5.2. Heat conduction in multi-bodies

To investigate the heat conduction capabilities of this model in both continuous (intragranular) and discontinuous (intergranular) media, a simulation was conducted to analyze the heat transfer process within a multi-body rock heap system. In this simulation, a rectangular container (0.5 m in width, and 0.7 m in height) with its base at a temperature of 100 °C and its two side panels at a temperature of 0 °C was studied, as shown in Fig. 5. Inside the container, 61 unevenly distributed rock blocks were placed, initially at a temperature of 0 °C, with an average size of 0.07 m. The entire model was divided into 3249 triangular elements. Table 2 lists the numerical setting parameters.

To quantitatively analyze the thermal field of the rock blocks within the container, a vertical straight monitoring line was positioned at a distance of 0.195 m from the left side panel. Additionally, 8 monitoring points were positioned around the line, as depicted in Fig. 5.

Fig. 6 illustrates the evolution of the thermal field within the multi-body system. Initially, a temperature rise was observed only in the bottom layer rock blocks directly in contact with the heating panel, as shown in Fig. 6a. Furthermore, due to varying contact areas between the bottom layer rocks and the heating panel, the rate of temperature increase differed. Rock blocks with larger contact areas exhibited a more pronounced temperature rise. As contact heat transfer continued (time steps ranging from 10,000 to 1,050,000), heat gradually propagated from the bottom to the top of the assembly, resulting in an overall temperature increase for all rock blocks within the container.

Fig. 7a depicts the evolution of temperature along the monitoring line, displaying a gradual increase in temperature from the bottom to the top. After 1,050,000 time steps, the temperature of the block located at the bottom of the multi-body system approaches 100 °C. In contrast, the temperature at the top of the multi-body system only begins to rise after 700,000 time steps, ultimately reaching 3.2 °C at 1,050,000 time steps.

Fig. 7b illustrates the evolution of temperatures at the monitoring points. At any given moment, the temperature is higher at the monitoring points closer to the heating plate, and lower at points farther away. The temperature at each monitoring point gradually incre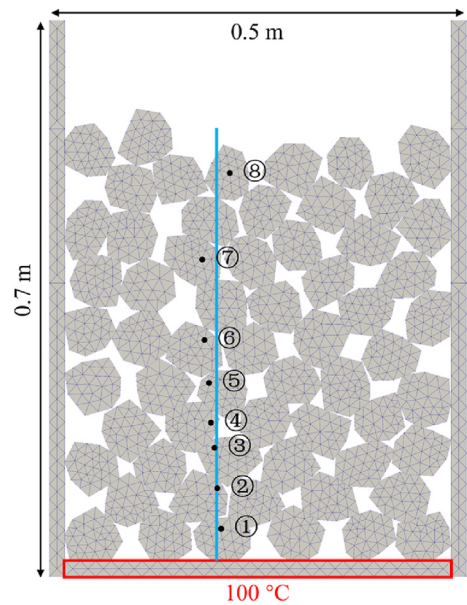ases over time, albeit with a diminishing rate of increase. Taking the lowest point, point 1, as an example, its temperature rises from 0 °C to 70 °C over 300,000 time steps, after which the rate of temperature increase ($dT/dt$) approaches zero. In summary, the simulation validates the reliability of the present
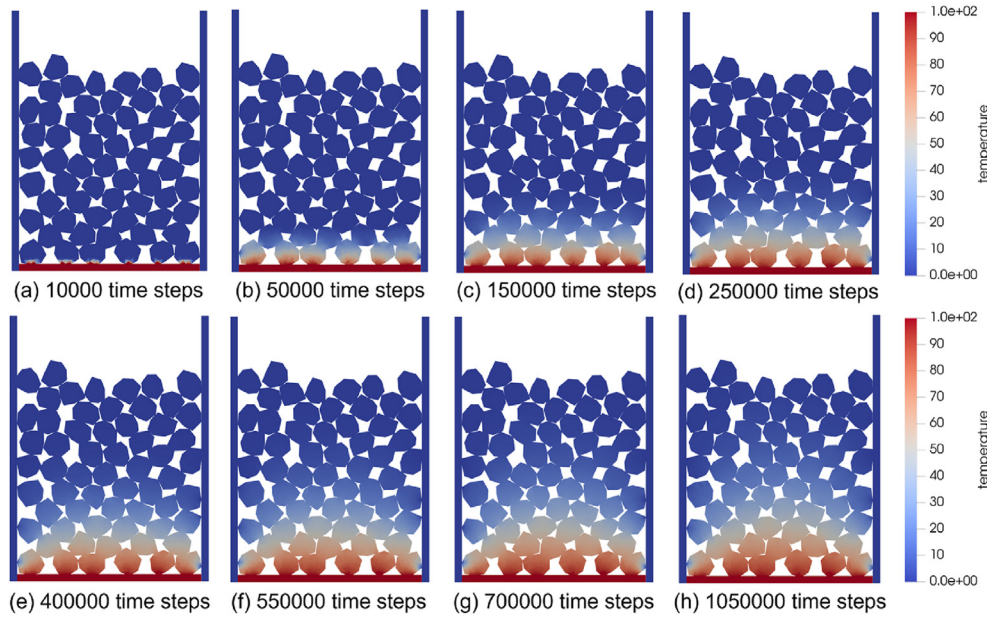


**Fig. 5.** Numerical model setup for heat conduction in multi-bodies.

**Table 2**
Numerical parameters of multi-bodies for transient heat conduction.

| Numerical parameter | Value |
|---|---|
| Mesh size (m) | ~0.015 |
| Time step (s) | $1 \times 10^{-7}$ |
| Density, $\rho$ (kg/m³) | 2500 |
| Elastic modulus, $E$ (GPa) | 10 |
| Poisson's ratio, $\nu$ | 0.25 |
| Thermal conductivity, $k$ (W/(m °C)) | 100 |
| Heat capacity, $c_p$ (J/(kg °C)) | 70 |
| $h_c$ | 0.5 |

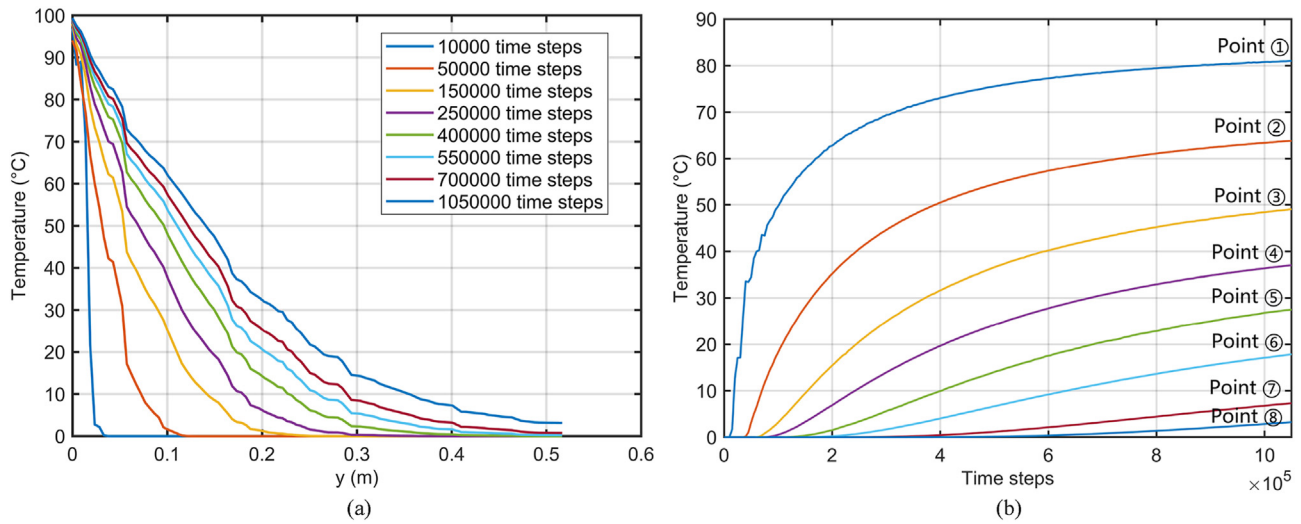**Fig. 6.** Heating up simulation of granular particles (unit: °C).



**Fig. 7.** Temperature distribution in multi-bodies: (a) Thermal field along the monitoring line at different time steps; and (b) Temperature evolution at the monitoring points with time.

thermal contact model in accurately simulating internal heat transferring within a multi-body system.

### 5.3. Stress and strain induced by temperature change

After verifying the reliability of the model in computing the thermal field, this case aims to validate its mechanical field accuracy. Assuming a square sheet with unconstrained boundaries and an initial temperature of $T_0$, applying a temperature difference $\Delta T$, the thermal strain/stress induced within the sheet due to temperature variation is calculated. The analytical solution for thermal stress and strain for this problem is shown below:

$$\left.\begin{aligned} \varepsilon_{xx} &= \varepsilon_{yy} = \alpha\Delta T \\ \sigma_{xx} &= \sigma_{yy} = \frac{E}{1-\nu}\alpha\Delta T \end{aligned}\right\} \quad (48)$$

**Table 3**
Numerical parameters for temperature change induced stress and strain simulation.

| Parameter | Value |
|---|---|
| Density, $\rho$ (kg/m$^3$) | 2300 |
| Elastic modulus, $E$ (GPa) | 75.1 |
| Poisson's ratio, $\nu$ | 0.311 |
| Tensile strength, $f_t$ (MPa) | 30 |
| Internal cohesion, $c$ (MPa) | 50 |
| Mode I fracture energy release rate, $G_I$ (J/m$^2$) | 100 |
| Mode II fracture energy release rate, $G_{II}$ (J/m$^2$) | 100 |
| Fracture penalty, $p_f$ (GPa) | 375 |
| Thermal conductivity, $k$ (W/(m °C)) | 2.6 |
| Heat capacity, $c_p$ (J/(kg °C)) | 700 |
| Thermal expansion coefficient, $\alpha$ ((°C)$^{-1}$) | $3 \times 10^{-6}$ |

Considering a square sheet with a length of 2 m, two transient temperature change conditions are taken into account: $\Delta T = 100$ °C

and $\Delta T = -100$ °C. The present TM coupled model is applied to simulate this problem, and the numerical model is discretized into 3708 triangular elements with an average element size of 0.05 m. The detailed mechanical and thermal parameters are provided in Table 3. Some parameters are determined according to the literature (Yan and Zheng, 2017; Wang et al., 2021).

Table 4 presents numerical simulation results for thermal strain and stress, which demonstrate good agreement with the analytical solutions. This agreement provides strong evidence for the accuracy of the coupled model in effectively addressing problems involving TM coupling. Fig. 8 presents a displacement vector diagram of the numerical simulation results. As shown in Fig. 8a, an increase in temperature leads to the outward expansion of the square sheet, with larger deformations observed at the outer boundaries, while the displacement at the center is the smallest. Conversely, Fig. 8b indicates that a decrease in temperature causes the square sheet to contract inward, resulting in greater deformations at the outer edges. Similarly, limited or even no displacement is observed at the center of the square plate. These findings qualitatively and quantitatively validate the effectiveness of this coupling model.



**Fig. 8.** Displacement vector diagram: (a) $\Delta T = 100$ °C; and (b) $\Delta T = -100$ °C.

### 5.4. Thermal stress in steady states

As shown in Fig. 9, for a hollow thick-walled cylinder with inner and outer radii $a$ and $b$, Dirichlet boundary conditions are applied at the inner and outer boundaries with temperatures of $T_a$ and $T_b$, respectively. Analytical solutions for temperature and stress in this problem can be found in the literature (Noda, 2018):

$$
\left.
\begin{array}{l}
T(r) = \dfrac{\ln(b/r)}{\ln(b/a)}T_a + \dfrac{\ln(a/r)}{\ln(a/b)}T_b \\[2ex]
\sigma_r(r) = \dfrac{E\alpha(T_a - T_b)}{2(1-\nu)}\left[\dfrac{\ln(b/r)}{\ln(b/a)} - \dfrac{b^2/r^2 - 1}{b^2/a^2 - 1}\right] \\[2ex]
\sigma_\theta(r) = \dfrac{E\alpha(T_a - T_b)}{2(1-\nu)}\left[\dfrac{\ln(b/r) - 1}{\ln(b/a)} + \dfrac{b^2/r^2 + 1}{b^2/a^2 - 1}\right]
\end{array}
\right\}
\tag{49}
$$

We utilize the current approach to simulate the problem and compare it with the analytical solutions. The discretization of the hollow cylinder is performed using 4927 triangular elements, as shown in Fig. 9. The simulation employs a time step of $8 \times 10^{-8}$ s. The TM parameters and boundary settings used in the simulation are shown in Table 5. The temperature, and radial and tangential thermal stresses after thermal stabilization of the system are depicted in Figs. 10–12, respectively. Notably, there is a significant consistency between the simulated results and analytical solutions, which attests to the capability of the proposed model in modeling coupled TM problems.
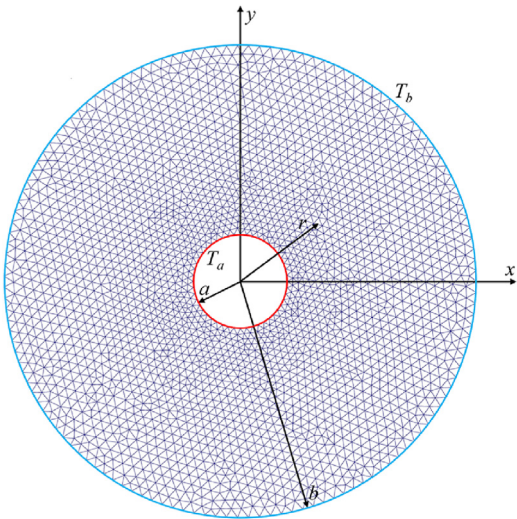


**Fig. 9.** Numerical model of the thick-wall cylinder.

**Table 5**
Mechanical and thermophysical parameters for hollow thick-walled cylinder.

| Numerical parameter | Value |
|---|---|
| Inner radius, $a$ (m) | 0.03 |
| Outer radius, $b$ (m) | 0.15 |
| Inner temperature (°C) | 100 |
| Outer temperature (°C) | 0 |
| Elastic modulus, $E$ (GPa) | 20 |
| Density, $\rho$ (kg/m$^3$) | 2500 |
| Poisson's ratio, $\nu$ | 0.2 |
| Thermal expansion coefficient, $\alpha$ ((°C)$^{-1}$) | $1.8 \times 10^{-5}$ |
| Heat capacity, $c_p$ (J/(kg °C)) | 10 |

### 5.5. Thermal fracturing validation

After validating the stress field against the analytical solution, the next step is to validate the thermal fracturing behavior. To
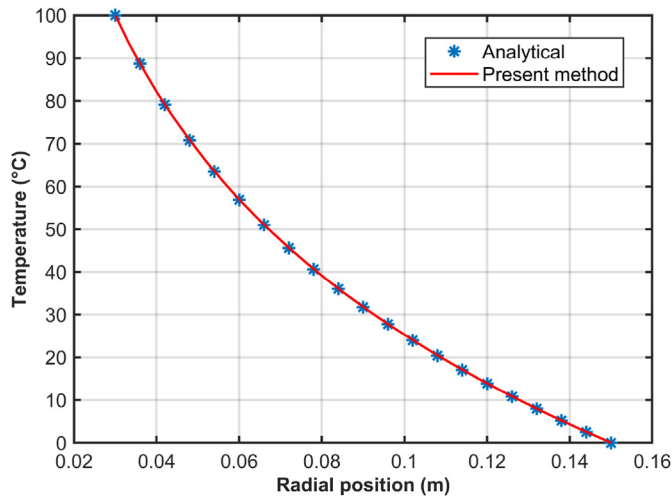
**Table 4**
Comparison of analytical and numerical solutions.

| Temperature (°C) | $\varepsilon_{xx}$ | | | $\varepsilon_{yy}$ | | | $\sigma_{xx}$ | | | $\sigma_{yy}$ | | |
|---|---|---|---|---|---|---|---|---|---|---|---|---|
| | Analytical | Numerical | Relative error (%) | Analytical | Numerical | Relative error (%) | Analytical (Pa) | Numerical (Pa) | Relative error (%) | Analytical (Pa) | Numerical (Pa) | Relative error (%) |
| 100 | $3 \times 10^{-4}$ | $2.9 \times 10^{-4}$ | 3.33 | $3 \times 10^{-4}$ | $2.9 \times 10^{-4}$ | 3.33 | $3.27 \times 10^7$ | $3.18 \times 10^7$ | 2.75 | $3.27 \times 10^7$ | $3.18 \times 10^7$ | 2.75 |
| −100 | $-3 \times 10^{-4}$ | $-2.9 \times 10^{-4}$ | 3.33 | $-3 \times 10^{-4}$ | $-2.9 \times 10^{-4}$ | 3.33 | $-3.27 \times 10^7$ | $-3.18 \times 10^7$ | 2.75 | $-3.27 \times 10^7$ | $-3.18 \times 10^7$ | 2.75 |

**Fig. 10.** Steady-state temperature distribution in the problem.
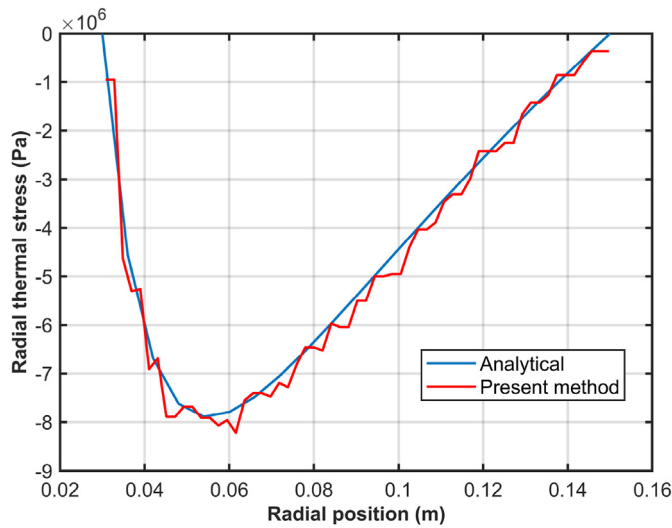


**Fig. 11.** Radial thermal stress $\sigma_r$ in the problem.
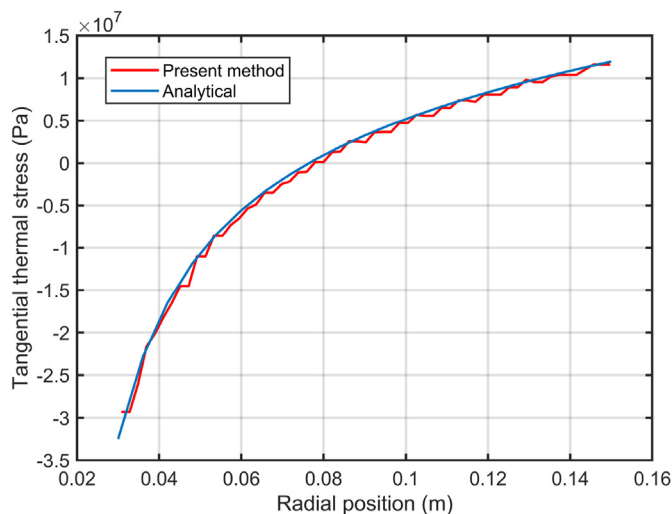


**Fig. 12.** Tangential thermal stress $\sigma_\theta$ in the problem.

achieve this, the hollow cylinder is discretized using a mesh composed of 3304 uniformly sized finite elements, each with a size of 0.007 m. Numerical computations are conducted with an integration time step of $1 \times 10^{-7}$ s. The specific material properties and boundary settings are provided in Table 6. Some parameters are determined based on the literature (Joulin et al., 2020; Wang et al., 2021).

The simulation results are represented in Fig. 13. The top row displays the maximal principal stress ($\sigma_1$), followed by the crack pattern in the second row, and the temperature field in the third row. Notably, the initial cracks emerge along the outer boundary of the cylinder and gradually extend towards the cylinder center. The observed fracture pattern closely resembles the experimental findings (Wanne and Young, 2008) depicted in Fig. 14, which also show straight fractures from the outer boundary to the center of the cylinder. The discrepancy in the number of cracks is primarily due to the heterogeneity of the experiment material.

### 5.6. Thermal shock-induced cracking

This section presents a simulation of a thermal shock-induced fracturing experiment. As depicted in Fig. 15a, several ceramic discs with a diameter of 13 mm and thickness of 1 mm were stacked together, with their upper and lower surfaces covered by two thick circular plates to prevent direct contact between the disc surfaces and water. The stacked discs are heated to the specified temperature and maintained at that temperature for 30 min. Four experimental groups are conducted at temperatures of 250 °C, 300 °C, 400 °C, and 500 °C, respectively. Subsequently, the heated discs are rapidly immersed in cold water (15 °C). This thermal shock exposure causes thermal cracks to initiate from the boundary and propagate towards the center of the specimen (Liu et al., 2015). Utilizing the current numerical model, thermal shock cracking behavior is studied through simulation of the experiment. A comparison is then conducted between the numerical results and the experimental findings. The numerical model is discretized using a total of 5020 uniform finite elements with a size of 0.0005 m, as depicted in Fig. 15b. The parameters utilized for the numerical case are presented in Table 7.

As depicted in Fig. 16, the temperature of the disc gradually decreases from the periphery towards the center, causing thermal shock-induced tensile stress fractures to initiate at the disc's periphery and develop centripetally in the radial direction. Fig. 17 shows that under various temperature conditions, the thermal shock fracture patterns in numerical simulations closely match those observed in experiments. The cracks are evenly distributed around the circumference, with their lengths alternating in a clockwise direction. Longer cracks are interspersed with shorter cracks. A quantitative comparison of the fracture quantities from numerical simulations and experiments is presented in Fig. 18. Both the experimental and simulation results demonstrate that the total

**Table 6**
Numerical parameters for thermal fracturing validation.

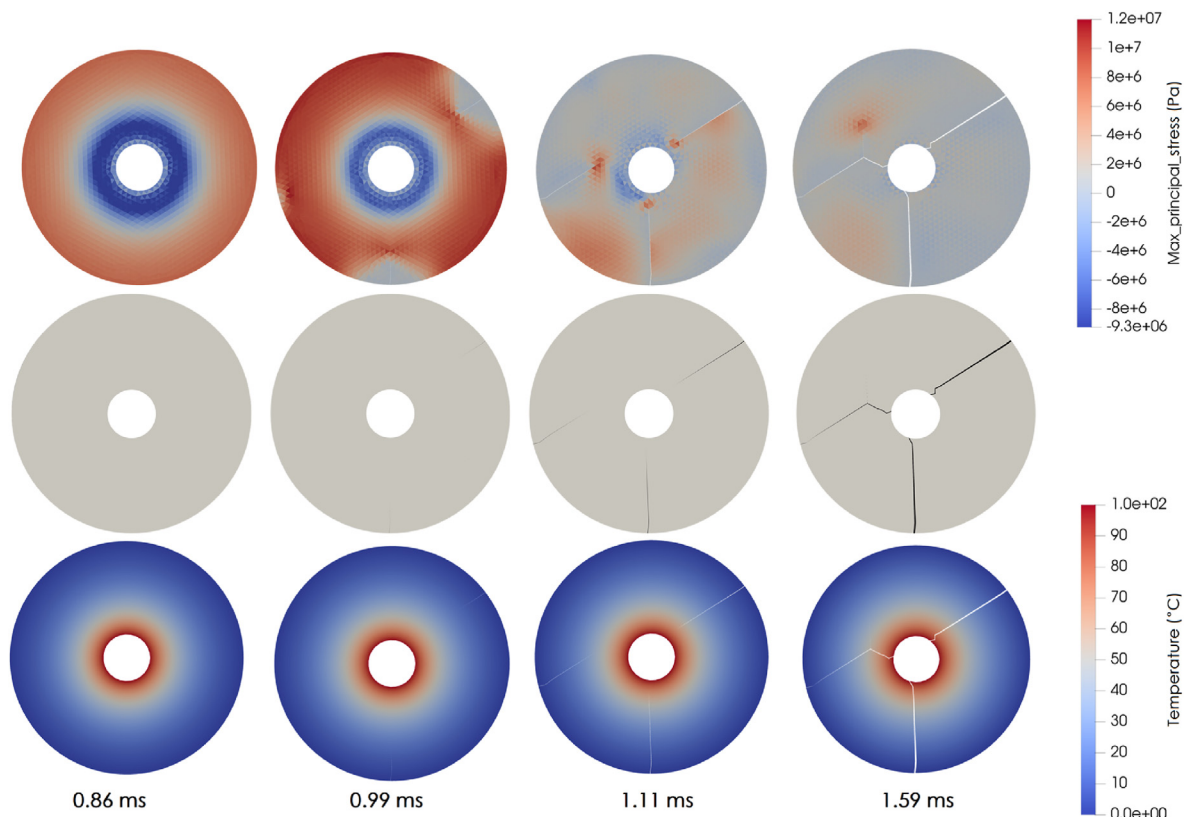| Parameters | Value |
|---|---|
| Elastic modulus, $E$ (GPa) | 20 |
| Poisson's ratio, $\nu$ | 0.25 |
| Density, $\rho$ (kg/m$^3$) | 2500 |
| Internal cohesion (MPa) | 20 |
| Tensile strength (MPa) | 10 |
| Fracture normal energy release rate (J/m$^2$) | 100 |
| Fracture shear energy release rate (J/m$^2$) | 100 |
| Fracture penalty number (GPa) | 100 |
| Thermal expansion coefficient, $\alpha$ ((°C)$^{-1}$) | $1.8 \times 10^{-5}$ |
| Heat capacity, $c_p$ (J/(kg °C)) | 10 |

**Fig. 13.** Numerical results of thermal cracks in the model (inner radius 0.03 m, and outer radius 0.15 m) at different times.
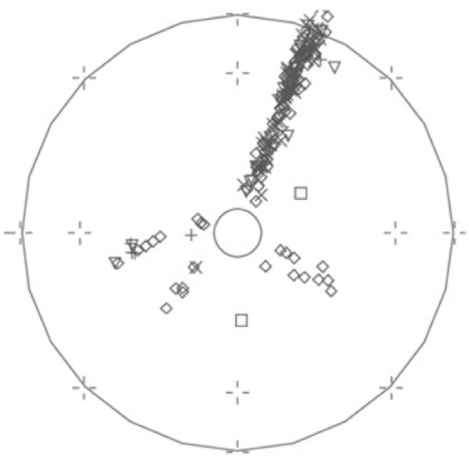


**Fig. 14.** Signals of acoustic emission associated with the thermal cracking of the hollow cylinder (inner radius 0.03 m, and outer radius 0.15 m) (Wanne and Young, 2008).



**Fig. 15.** Diagram of the thermal shock specimen: (a) Experiment setting; and (b) Numerical model meshing scheme.

**Table 7**
Numerical parameters for thermal shock-induced cracking.

| Parameter | Value |
|---|---|
| Elastic modulus, $E$ (GPa) | 370 |
| Poisson's ratio, $\nu$ | 0.22 |
| Density, $\rho$ (kg/m$^3$) | 3980 |
| Tensile strength (MPa) | 180 |
| Thermal conductivity (W/(m °C)) | 35 |
| Heat capacity (J/(kg °C)) | 850 |
| Thermal expansion coefficient, $\alpha$ ((°C)$^{-1}$) | $7.5 \times 10^{-5}$ |

number of fractures increases as the maximum heating temperature rises.

## 6. Discussion

The benefit of using TM coupling models lies in their ability to incorporate the effects of temperature on the mechanical properties of geomaterials in geological engineering research (Abdollahipour and Fatehi Marji, 2020). Some insights are provided by the present study.

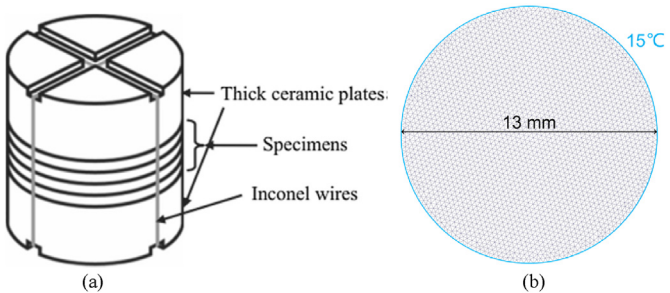From the microscopic perspective in Section 5.3, temperature increase and decrease will cause the microelements of material to expand and contract, respectively. However, if the deformation of microelements is restrained, such a tendency of expansion and contraction will induce extra compressive and tensile stress inside the material. Generally, geomaterials are susceptible to tensile stress, and thus, even small tensile stress will cause damage, like microcracks, to the material. It is well documented that
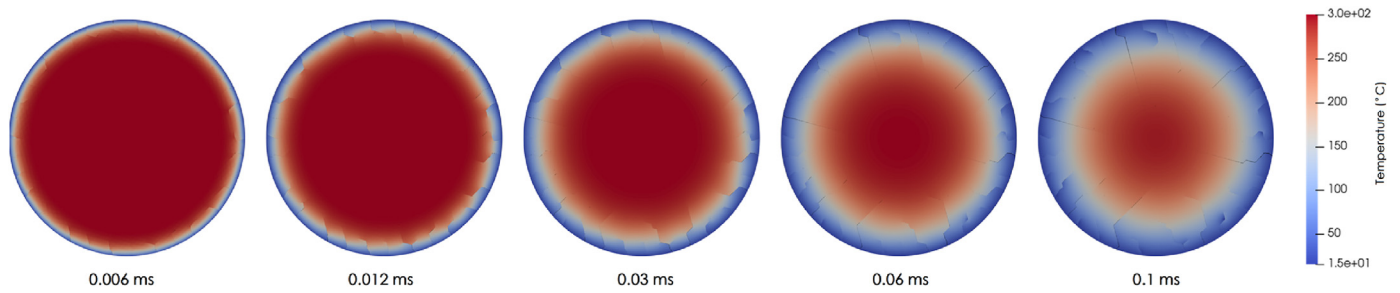
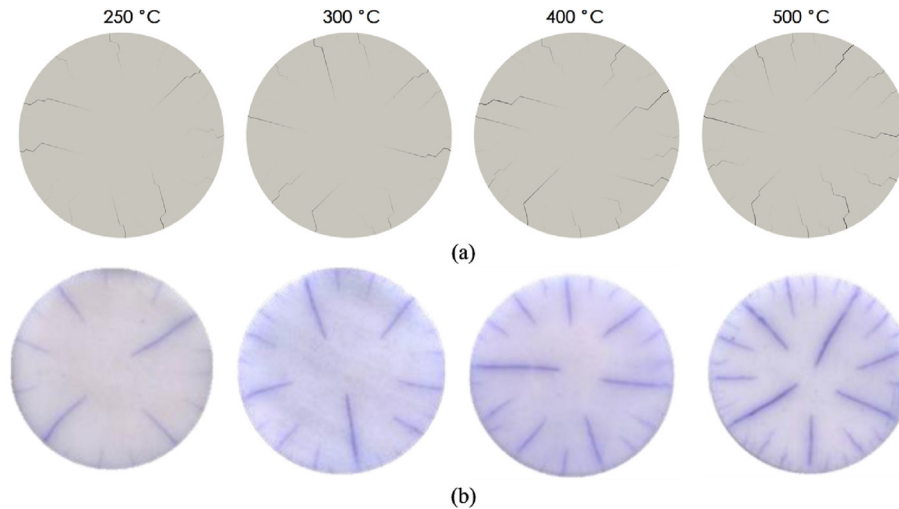**Fig. 16.** Thermal shocking crack propagation process.



**Fig. 17.** Comparison of crack pattern: (a) Results of present method; and (b) Experimental results (Liu et al., 2015).

macroscopic mechanical parameters, such as elastic modulus and strength, are affected by the internal damage of the material (Haeri et al., 2014). Therefore, a restrained cooling process will lead to the degradation of macroscopic mechanical parameters of geomaterials.

On the other hand, the expansion behavior resulting from temperature increases can have both positive and negative effects on geomaterials. For instance, in the case of rocks, the initial mineral particle expansion leads to the closure of microcracks and micropores, and an increase in the normal stress along particle interfaces. Consequently, the mechanical properties of rocks may experience a slight improvement under a mild temperature range (from room temperature to 200 °C), as has been well articulated by Wong et al. (2020). However, if the temperature keeps increasing, the thermal expansion mismatch among mineral particles can generate tensile or shear stress within the materials. Once these stresses reach a critical level, the material's integrity becomes compromised, resulting in a decline in mechanical properties.

From the macroscopic perspective, as discussed in Sections 5.5 and 5.6, the thermal gradient caused by temperature increase and decrease can result in additional stresses and the formation of fractures within the material. Consequently, the mechanical properties may become compromised or even lost due to these macroscopic fractures.

The above findings and insights suggest that the present TM coupling model, which accounts for the effects of temperature on the mechanical properties of geomaterials from perspectives of both microscopic mechanisms and the macroscopic phenomena, holds promise for further research in temperature-sensitive
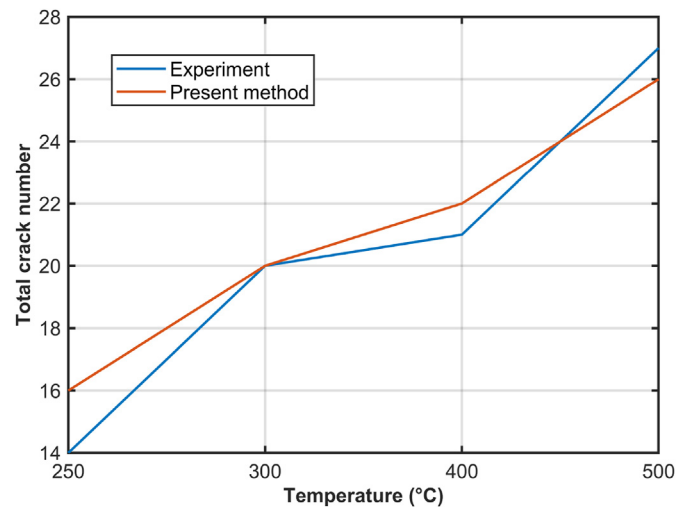


**Fig. 18.** Thermal shock-induced crack quantity of numerical and experimental results at various maximum temperatures.

engineering applications such as HDR, deep oil reservoirs, and geological disposal of radioactive waste. Investigating the impact of temperature on the macroscopic mechanical properties of geomaterials is a complex and intricate issue. A systematic approach to studying this problem, which combines multiple experimental methods combined with the present TM coupling model, will be the future research direction.

## 7. Conclusions

Recognizing the significant potential of FDEM in simulating geotechnical engineering problems, a novel TM coupled FDEM has been proposed for geomaterials, incorporating heat conduction, thermal cracking, and contact heat transfer. The following conclusions can be drawn:

(1) To ensure precise calculation of the temperature field under quasi-static and dynamic conditions, a heat conduction model accounting for continuous-discontinuous transition processes within a finite element framework is incorporated, together with the modified contact heat transfer model that integrates the entire contact area of discrete bodies.

(2) To align with the finite strain theory used in the FDEM mechanics module, the TM coupling module in the model is based on the multiplicative decomposition of the deformation gradient.

(3) The TM coupled FDEM model was applied to simulate various scenarios, such as heat conduction in both continuous and discontinuous materials under transient states, thermally induced strain and stress, and thermal cracking problems.

(4) To validate the accuracy of the thermal field calculation model and the TM coupling model, the numerical results were compared with experimental findings and analytical solutions, demonstrating good agreement. These numerical examples convincingly demonstrate the robust reliability of the proposed model, making it suitable for versatile applications across a broad range of continuous and discontinuous geomaterials.

## Declaration of competing interest

The authors declare that they have no known competing financial interests or personal relationships that could have appeared to influence the work reported in this paper.

## Acknowledgments

## References

Abdollahipour, A., Fatehi Marji, M., 2020. A thermo-hydromechanical displacement discontinuity method to model fractures in high-pressure, high-temperature environments. Renew. Energy 153, 1488−1503.

Abdollahipour, A., Fatehi Marji, M., Yarahmadi, B.A., Gholamnejad, J., 2016a. Numerical investigation of effect of crack geometrical parameters on hydraulic fracturing process of hydrocarbon reservoirs. J. Min. Environ. 7 (2), 205−214.

Abdollahipour, A., Fatehi Marji, M., Bafghi, A.Y., Gholamnejad, J., 2016b. A complete formulation of an indirect boundary element method for poroelastic rocks. Comput. Geotech. 74, 15−25.

André, D., Levraut, B., Tessier-Doyen, N., Huger, M., 2017. A discrete element thermo-mechanical modelling of diffuse damage induced by thermal expansion mismatch of two-phase materials. Comput. Methods Appl. Mech. Eng. 318, 898−916.

Bazazzadeh, S., Mossaiby, F., Shojaei, A., 2020. An adaptive thermo-mechanical peridynamic model for fracture analysis in ceramics. Eng. Fract. Mech. 223, 106708.

Cai, W., Gao, K., Ai, S., Wang, M., Feng, Y.T., 2023. Implementation of extrinsic cohesive zone model (ECZM) in 2D finite-discrete element method (FDEM) using node binding scheme. Comput. Geotech. 159, 105470.

Choo, L.Q., Zhao, Z., Chen, H., Tian, Q., 2016. Hydraulic fracturing modeling using the discontinuous deformation analysis (DDA) method. Comput. Geotech. 76, 12−22.

Cui, X., Wong, L.N.Y., 2022. A 3D fully thermo−hydro−mechanical coupling model for saturated poroelastic medium. Comput. Methods Appl. Mech. Eng. 394, 114939.

Fu, J., Haeri, H., Sarfarazi, V., Asgari, K., Ebneabbasi, P., Fatehi Marji, M., Guo, M., 2022. Extended finite element method simulation and experimental test on failure behavior of defects under uniaxial compression. Mech. Adv. Mater. Struct. 29 (27), 6966−6981.

Fukuda, D., Mohammadnejad, M., Liu, H., Zhang, Q., Zhao, J., Dehkhoda, S., Chan, A., Kodama, J., Fujii, Y., 2020. Development of a 3D hybrid finite-discrete element simulator based on GPGPU-parallelized computation for modelling rock fracturing under quasi-static and dynamic loading conditions. Rock Mech. Rock Eng. 53 (3), 1079−1112.

Giannopoulos, G.I., Anifantis, N.K., 2005. Thermal fracture interference: a two-dimensional boundary element approach. Int. J. Fract. 132, 351−369.

Guo, P., Zhang, P., Bu, M., Wang, J., Zheng, X., He, M., 2023. Microcracking behavior and damage mechanism of granite subjected to high temperature based on CT-GBM numerical simulation. Comput. Geotech. 159, 105385.

Haeri, H., Shahriar, K., Marji, M.F., Moarefvand, P., 2013. Simulating the bluntness of TBM disc cutters in rocks using displacement discontinuity method. In: Proceedings of the 13th International Conference on Fracture, Beijing, China.

Haeri, H., Shahriar, K., Marji, M.F., Moarefvand, P., 2014. Experimental and numerical study of crack propagation and coalescence in pre-cracked rock-like disks. Int J. Rock Mech. Min. Eng. 67, 20−28.

Jiao, Y., Zhang, X., Zhang, H., Li, H., Yang, S., Li, J., 2015. A coupled thermo-mechanical discontinuum model for simulating rock cracking induced by temperature stresses. Comput. Geotech. 67, 142−149.

Joulin, C., Xiang, J., Latham, J., 2020a. A novel thermo-mechanical coupling approach for thermal fracturing of rocks in the three-dimensional FDEM. Comput. Part. Mech. 7 (5), 935−946.

Joulin, C., Xiang, J., Latham, J., Pain, C., Salinas, P., 2020b. Capturing heat transfer for complex-shaped multibody contact problems, a new FDEM approach. Comput. Part. Mech. 7 (5), 919−934.

Li, Y., Yu, T., Natarajan, S., 2022. An adaptive isogeometric phase-field method for brittle fracture in rock-like materials. Eng. Fract. Mech. 263, 108298.

Liu, P., Yu, T., Bui, T.Q., Zhang, C., Xu, Y., Lim, C.W., 2014. Transient thermal shock fracture analysis of functionally graded piezoelectric materials by the extended finite element method. Int. J. Solid Struct. 51 (11−12), 2167−2182.

Liu, Y., Wu, X., Guo, Q., Jiang, C., Song, F., Li, J., 2015. Experiments and numerical simulations of thermal shock crack patterns in thin circular ceramic specimens. Ceram. Int. 41 (1), 1107−1114.

Mahabadi, O.K., Lisjak, A., Munjiza, A., Grasselli, G., 2012. Y-Geo: new combined finite-discrete element numerical code for geomechanical applications. Int. J. GeoMech. 12 (6), 676−688.

Miehe, C., Hofacker, M., Schänzel, L., Aldakheel, F., 2015a. Phase field modeling of fracture in multi-physics problems. Part II. Coupled brittle-to-ductile failure criteria and crack propagation in thermo-elastic-plastic solids. Comput. Methods Appl. Mech. Eng. 294, 486−522.

Miehe, C., Schaenzel, L., Ulmer, H., 2015b. Phase field modeling of fracture in multi-physics problems. Part I. Balance of crack surface and failure criteria for brittle crack propagation in thermo-elastic solids. Comput. Methods Appl. Mech. Eng. 294, 449−485.

Munjiza, A., Andrews, K., 1998. NBS contact detection algorithm for bodies of similar size. Int. J. Numer. Methods Eng. 43 (1), 131−149.

Munjiza, A., Owen, D.R.J., Bicanic, N., 1995. A combined finite-discrete element method in transient dynamics of fracturing solids. Eng. Comput. 12 (2), 145−174.

Noda, N., 2018. Thermal Stresses, second ed. Routledge, New York, USA.

Rinne, M., Shen, B., Backers, T., 2013. Modelling fracture propagation and failure in a rock pillar under mechanical and thermal loadings. J. Rock Mech. Geotech. Eng. 5 (1), 73−83.

Shahami, M.H., Bafghi, A.Y., Marji, M.F., 2019. Investigating the effect of external forces on the displacement accuracy of discontinuous deformation analysis (DDA) method. Comput. Geotech. 111, 313−323.

Sun, L., Liu, Q., Grasselli, G., Tang, X., 2020. Simulation of thermal cracking in anisotropic shale formations using the combined finite-discrete element method. Comput. Geotech. 117, 103237.

Sun, L., Liu, Q., Tao, S., Grasselli, G., 2022. A novel low-temperature thermo-mechanical coupling model for frost cracking simulation using the finite-discrete element method. Comput. Geotech. 152, 105045.

Tang, S.B., Zhang, H., Tang, C.A., Liu, H.Y., 2016. Numerical model for the cracking behavior of heterogeneous brittle solids subjected to thermal shock. Int. J. Solid Struct. 80, 520−531.

Vujosevic, L., Lubarda, V.A., 2002. Finite-strain thermoelasticity based on multiplicative decomposition of deformation gradient. Theor. Appl. Mech. (28−29), 379−399.

Wang, Y., Zhou, X., Kou, M., 2018. A coupled thermo-mechanical bond-based peridynamics for simulating thermal cracking in rocks. Int. J. Fract. 211 (1−2), 13−42.

Wang, Z., Liu, Q., Wang, Y., 2021. Thermo-mechanical FDEM model for thermal cracking of rock and granular materials. Powder Technol. 393, 807−823.

Wanne, T.S., Young, R., 2008. Bonded-particle modeling of thermally fractured granite. Int J. Rock Mech. Min. Eng. 45 (5), 789−799.

Wong, L., Zhang, Y., Wu, Z., 2020. Rock strengthening or weakening upon heating in the mild temperature range? Eng. Geol. 272, 105619.

Wu, D., Li, H., Fukuda, D., Liu, H., 2023. Development of a finite-discrete element method with finite-strain elasto-plasticity and cohesive zone models for simulating the dynamic fracture of rocks. Comput. Geotech. 156, 105271.

Wu, Z., Cui, W., Weng, L., Liu, Q., 2022. A 2D FDEM-based THM coupling scheme for modeling deformation and fracturing of the rock mass under THM effects. Comput. Geotech. 152, 105019.

Xia, M., 2015. Thermo-mechanical coupled particle model for rock. Trans. Nonferrous Metals Soc. China 25 (7), 2367–2379.

Xiang, J., Munjiza, A., Latham, J., 2009. Finite strain, finite rotation quadratic tetrahedral element for the combined finite-discrete element method. Int. J. Numer. Methods Eng. 79 (8), 946–978.

Yan, C., Jiao, Y., 2020. A 2D discrete heat transfer model considering the thermal resistance effect of fractures for simulating the thermal cracking of brittle materials. Acta Geotech 15 (5), 1303–1319.

Yan, C., Zheng, H., 2017. A coupled thermo-mechanical model based on the combined finite-discrete element method for simulating thermal cracking of rock. Int J. Rock Mech. Min. Eng. 91, 170–178.

Yan, C., Jiao, Y.Y., Zheng, H., 2019b. A three-dimensional heat transfer and thermal cracking model considering the effect of cracks on heat transfer. Int. J. Numer. Anal. Methods GeoMech. 43 (10), 1825–1853.

Yan, C., Ren, Y., Yang, Y., 2019a. A 3D thermal cracking model for rock based on the combined finite–discrete element method. Comput. Part. Mech. 7, 881–901.

Yan, C., Yang, Y., Wang, G., 2021a. A new 2D continuous-discontinuous heat conduction model for modeling heat transfer and thermal cracking in quasi-brittle materials. Comput. Geotech. 137, 104231.

Yan, C., Zheng, Y., Huang, D., Wang, G., 2021b. A coupled contact heat transfer and thermal cracking model for discontinuous and granular media. Comput. Methods Appl. Mech. Eng. 375, 113587.

Zeng, Q., Yao, J., Shao, J., 2020. An extended finite element solution for hydraulic fracturing with thermo-hydro-elastic–plastic coupling. Comput. Methods Appl. Mech. Eng. 364, 112967.

Zhao, Q., Lisjak, A., Mahabadi, O., Liu, Q., Grasselli, G., 2014. Numerical simulation of hydraulic fracturing and associated microseismicity using finite-discrete element method. J. Rock Mech. Geotech. Eng. 6 (6), 574–581.

**Louis Ngai Yuen Wong** is a Professor of Engineering Geology at the University of Hong Kong (HKU), China. He earned his BSc degree in Earth Sciences from HKU and later pursued his doctoral and post-doctoral studies in Geotechnical Engineering at the prestigious Massachusetts Institute of Technology (MIT), USA. Before joining HKU, he held the positions of Assistant Professor and Assistant Chair (Academic) in the School of Civil and Environmental Engineering at Nanyang Technological University in Singapore. His research, which encompasses both experimental and numerical approaches, aims to enhance the understanding of rock deformation and apply this knowledge to various societal applications, including underground construction, energy exploration, and earthquake studies. He received the Richard Wolters' Prize from the International Association of Engineering Geology and Environment (IAEG) in 2014. Since 2018, he has been serving as the Editor-in-Chief of the *Bulletin of Engineering Geology and the Environment.*